

**The coupled stratosphere-troposphere response to  
impulsive forcing from the troposphere**

*Thomas Reichler*

Geophysical Fluid Dynamics Laboratory / Princeton University, Princeton

*Paul J. Kushner*

Department of Physics / University of Toronto, Toronto

*Lorenzo M. Polvani*

Dept. of Applied Physics and Applied Mathematics / Columbia University, New York

Correspondence to: Thomas Reichler ([reichler@princeton.edu](mailto:reichler@princeton.edu))

Draft from Thursday, June 03, 2004

## Table of Contents

|  |           |
|--|-----------|
| Abstract.....  | 3         |
| <b>1. Introduction .....</b>                         | <b>3</b>  |
| <b>2. Model and design of the integrations .....</b> | <b>6</b>  |
| a. Model description .....                           | 6         |
| b. Perturbation integrations .....                   | 7         |
| <b>3. Results .....</b>                              | <b>9</b>  |
| a. Ensemble-mean response .....                      | 9         |
| b. Classification of the realizations.....           | 11        |
| c. Predictors of the tropospheric response .....     | 14        |
| d. An independent test of the predictors.....        | 16        |
| e. Dynamical interpretation.....                     | 17        |
| <b>4. Conclusion.....</b>                            | <b>18</b> |
| Appendix: Forcing of the model .....                 | 20        |
| References.....                                      | 22        |
| Figure Captions .....                                | 26        |

## **Abstract**

In order to understand the dynamics of stratosphere-troposphere coupling, a simple atmospheric general circulation model (GCM) is used to investigate the transient response of the stratosphere-troposphere system to externally imposed pulses of lower-tropospheric planetary wave activity. The atmospheric GCM is a dry, hydrostatic, global primitive-equations model, whose circulation includes an active polar vortex and a tropospheric jet maintained by baroclinic eddies. Planetary wave activity pulses are generated by a perturbation of the solid lower boundary that grow and decay over a period of ten days. The planetary wave pulses propagate upward and break in the stratosphere. Subsequently, a zonal-mean circulation anomaly propagates downward, often into the troposphere, at lags of 30 to 100 days. The evolution of the response is found to be dependent on the state of the stratosphere-troposphere system at the time the pulse is generated. In particular, on the basis of a large ensemble of these simulations, we find that the length of time the signal takes to propagate downward from the stratosphere is controlled by initial anomalies in the zonal-mean circulation and in the zonal-mean wave drag. Criteria based on these anomaly patterns can be used, therefore, to predict the long-term surface response of the stratosphere-troposphere system to a planetary wave pulse up to 90 days after the pulse is generated. In an independent test, we verify that the initial states that most strongly satisfy these criteria respond in the expected way to the lower tropospheric wave-activity pulse.

## **1. Introduction**

In this study, we explore, with an idealized model, the dynamics of extratropical zonal-mean flow anomalies that are observed to propagate downward from the stratosphere into the troposphere (Baldwin and Dunkerton 1999, 2001). These signals, which we will

hereafter call “troposphere-stratosphere-troposphere” or “TST” events, have attracted attention because of their connections to multiple-week tropospheric circulation forecasts (Baldwin and Dunkerton 2001, Baldwin et al. 2003, Charlton et al. 2004) and to the long-term mean circulation response to climate change (Thompson and Solomon 2002, Gillett and Thompson 2003). The cause of TST events are planetary waves that propagate up from the troposphere, dissipate and mix potential vorticity (PV) in the stratosphere, and bring about a mean flow and residual circulation response there (e.g. Charney and Drazin 1961, Polvani and Waugh 2004). But the dynamics of the subsequent evolution of the TST events is still unclear and raises the question of just how the stratosphere might “influence” the tropospheric circulation (Baldwin et al. 2003).

Various ideas have been put forward to explain the dynamics of TST signals, including PV inversion (Black 2002, Ambaum and Hoskins 2002), eddy mean-flow interaction and downward-control (Dickinson 1968, Haynes et al. 1991, Holton and Mass 1976, Plumb and Semeniuk 2003), and planetary-wave reflection in the stratosphere (Perlwitz and Harnik 2003). Each of these ideas leads to different conclusions about the nature of the stratospheric influence. One step towards resolving these differences is to construct a relatively simple modeling framework that cleanly separates stratospheric from tropospheric influences. Without such a framework, the way the stratosphere might control, for example, the upward flux of wave activity from the troposphere that initiates the TST events remains ambiguous.

In this study, we investigate the lifecycle of TST events by explicitly generating them in the lower troposphere of a relatively simple atmospheric general circulation model (GCM) of the stratosphere-troposphere system. This is in contrast to approaches in which

the stratosphere is perturbed directly (e.g. Christiansen 2003, Charlton et al. 2004, Song and Robinson 2004) or in which the tropopause is perturbed and the troposphere is not modeled (e.g. Holton and Mass 1976, Plumb and Semeniuk 2003, Polvani and Saravanan 2000). The atmospheric GCM is the same dry, hydrostatic general circulation model that two of us have used in previous studies of stratosphere-troposphere dynamics (Polvani and Kushner 2002, hereafter PK; Kushner and Polvani 2004, hereafter KP). Our approach is illustrated schematically in Fig. 1: starting from a spun-up atmospheric initial condition, a pulse of lower-tropospheric wave activity is generated over a period of 10 days by perturbing the solid lower boundary; the pulse propagates into the stratosphere and breaks, and the subsequent evolution of zonal flow anomalies is examined. This subsequent evolution often, but not always, yields downward propagation of the zonal flow anomalies into the troposphere, that is, complete TST events. The atmospheric response, especially long after the initial pulse is generated, is highly variable and depends strongly on the initial state of the atmosphere. We find that, although the initial driver of the perturbation is unambiguously tropospheric, the subsequent evolution of the perturbation can be influenced by stratospheric conditions. The objective of this study is to identify predictors of the long-term response. Ultimately, we wish to understand the response in light of the dynamical literature cited above.

In what follows, we first describe the model and the design of the numerical integrations (Section 2) and then the results of a large ensemble of these pulse calculations (Section 3a). We next develop a classification technique to categorize the range of possible responses (Section 3b), discuss predictors of the response (Section 3c), and present a dynamical interpretation of those predictors (Section 3d). We conclude with a discussion

of these results and another sensitivity study (Section 4). In the appendix, we provide additional technical details related to the forcing of the model.

## 2. Model and design of the integrations

### *a. Model description*

Our model is a slightly modified version of the one used by PK and KP; the reader is referred to these papers for further details. It solves the dry, hydrostatic, primitive equations on the sphere and uses the Held and Suarez (1994, hereafter HS) prescription for Newtonian cooling in the troposphere, the PK prescription for Newtonian cooling in the stratosphere, and Rayleigh damping of the zonal and meridional winds in the planetary boundary layer and in a sponge above 0.5 hPa (explicit formulas of the forcing functions are provided in the appendix). We use T42 spectral resolution in the horizontal and 40  $\sigma$ -level resolution in the vertical; the vertical levels extend from the ground to the mesosphere. The simulation represents perpetual solstitial conditions.

We note the following differences between our model and PK/KP's model. First, in our model, the tropospheric Newtonian-cooling profile matches that of HS. This is achieved by setting the parameter  $\epsilon$  in equation (A9), which controls the asymmetry of the tropospheric temperature gradients between the hemispheres, to zero. Second, in the standard-runs of our model, we use a stratospheric Newtonian damping timescale of 20 d, which is half the value of that used in PK, KP, and HS. This shorter damping time scale effectively strengthens the stratosphere-troposphere coupling in the model. See Section 4 for further discussion of this. Finally, in our standard-runs, the parameter  $\gamma$ , which controls the strength of the stratospheric winter hemisphere temperature gradients (PK), is set to 1. This makes the polar vortex relatively weak compared to the  $\gamma = 2$  and  $\gamma = 4$  cases studied

in PK, and thus increases the amount of wave-activity absorption and stratosphere-troposphere coupling.

The zonal- and time-mean zonal-winds for our control-run, which is integrated for approximately 40,000 d after a 1,000 d spin-up period, is plotted in Fig. 2a. The model produces a fairly realistic zonal wind profile, with an active baroclinic-eddy-driven jet in the troposphere, a stratospheric polar vortex, and tropical easterlies. The maximum zonal velocities in the polar vortex reach 57 m/s, which is close to the observed solstitial winds as shown, for example, in Fig. 1.4 of Andrews et al. (1987). As in PK and KP, the model has a flat lower boundary and forcing and dissipation terms that are zonally homogenous. Therefore, the model has no stationary eddies: the extratropical circulation is maintained by transient baroclinic eddies in the troposphere and by transient planetary eddies in the stratosphere (Scinocca and Haynes 1998).

Below, we refer to the model's annular mode (AM), whose spatial structure is shown in Fig. 2b. To obtain this figure, we first find the leading principal component time series of the 853 hPa zonal-mean geopotential height poleward of 20N, after it has been multiplied by the square root of the cosine of latitude. The principal component time series is then divided by its standard deviation, to yield a quantity with unit standard deviation. Fig. 2b shows the covariance or regression of the zonal-mean geopotential with the resulting quantity. In the troposphere and lower stratosphere, the mode consists of a meridional dipole that is similar to observations (Baldwin and Dunkerton 1999).

#### *b. Perturbation integrations*

To generate TST events, we next perform an ensemble of perturbation integrations that branch from the control-run at 100 d intervals. Using the control-run initial condition

as a starting point, a pulse of upward propagating planetary wave activity is generated by specifying that the surface geopotential  $\Phi_s$  vary as a function of space and time according to the expression

$$\Phi_s(\lambda, \varphi, t) = \eta(\lambda, \varphi)T(t) \quad (1)$$

where  $\lambda$  is longitude,  $\varphi$  is latitude, and  $t$  is time, the shape of the perturbation is given by

$$\eta(\lambda, \varphi) = \begin{cases} A_0 \sin^2\left(\frac{\varphi - \varphi_0}{\varphi_1 - \varphi_0}\pi\right) \cos(k\lambda) & \varphi_0 \leq \varphi \leq \varphi_1 \\ 0 & \text{else} . \end{cases} \quad (2)$$

and the temporal evolution of the surface geopotential perturbation is given by

$$T(t) = \begin{cases} \sin^2 \frac{t\pi}{\Delta t} & t \leq \Delta t \\ 0 & t > \Delta t , \end{cases} \quad (3)$$

The parameters we use for our standard-runs are  $k = 1$ ,  $A_0 = 5000$  m,  $\varphi_l = 40^\circ\text{N}$ ,  $\varphi_2 = 80^\circ\text{N}$ , which represents a wavenumber 1 sinusoidal perturbation centered at  $60^\circ\text{N}$ , a zero mean, and a peak-to-trough displacement of 10,000 m. The time envelope parameter  $\Delta t = 10$  days. This parameter setting as well as the parameters that control the mean state of the polar vortex (i.e.,  $\gamma$  and  $k_{st}$ , see appendix) were chosen with a heuristic goal in mind. Based on an initial sensitivity study, in which these parameter were varied, we found that this particular combination led to a reasonably strong upward propagating signal, a physically plausible stratospheric response, and a relatively large fraction of cases with well defined TST events.



After the initial 10 day long forcing period, the model is integrated with  $\Phi_s = 0$  for 90 more days to investigate the response of the system to the imposed forcing. Apart from the perturbation of the lower surface for the first 10 days, the perturbation-runs are identical to the control-run. We conduct a total of 403 perturbation integrations, which define our ensemble.

### 3. Results

#### *a. Ensemble-mean response*

Fig. 3 shows the ensemble-mean departure of the 116 hPa geopotential height from the control-run mean at day 8, which represents the time of the peak response to the lower-tropospheric wave activity pulse at this level. Since the surface forcing reaches its peak at day 5, we see that it takes roughly 3 days for the waves to travel to this level. As one would expect from the structure of the forcing function, the main component of the lower stratospheric response is a zonal wave number one perturbation, which is confined roughly to latitudes north of 30°N. The anomalies are between  $-400$  and  $+600$  meters, which is similar to the observed lower stratospheric geopotential height anomalies during strong sudden warming events (e.g. Matsuno 1971, McIntyre and Palmer 1984, Andrews et al. 1987, Baldwin and Dunkerton 1989). This confirms that the externally imposed pulse of tropospheric wave activity leads to a plausible atmospheric response.

As expected by the design of our setup, the upward propagating planetary wave pulse is sufficiently strong to cause significant warming and irreversible potential vorticity (PV) mixing in the stratosphere. Fig. 4 shows the northern hemisphere 950 K (ca. 5 hPa or 35 km) PV distribution for the control-run time-mean (Fig. 4a) and for the day-15 perturbation-run ensemble-mean (Fig. 4b). By day 15, which represents the time of the

peak response at this level, there has been a net southward flux of PV, shown as a decrease of PV over higher latitudes and an increase over low latitudes. The ensemble-mean perturbation PV structure of the polar vortex shows a displacement off the pole (corresponding to a wavenumber 1 anomaly) and elongation (wavenumber 2). When we examine individual realizations, we find that the ensemble-mean picture does represent typical distortions seen in the polar vortex as a result of the wave-activity pulse.

Figs. 3 and 4 confirm that the externally imposed tropospheric wave-activity pulse leads to a plausible stratospheric response on a time scale of about two weeks. Our primary interest here, however, is in the subsequent evolution of the stratosphere-troposphere system. Fig. 5 shows a measure of the geopotential response over the polar cap as a function of time and pressure. The quantity plotted is

$$R = \frac{\langle \Phi \rangle' (p, t)}{s_{ctl}(\langle \Phi \rangle)(p)} \quad (4)$$

where  $\langle \Phi \rangle$  represents the zonal- and 60N-90N meridional-mean of the geopotential,  $\langle \Phi \rangle'$  represents the difference between the instantaneous value of  $\langle \Phi \rangle$  in an individual realization and the control-run time-mean value of  $\langle \Phi \rangle$ , and  $s_{ctl}(\langle \Phi \rangle)$  represents the control-run daily standard deviation of  $\langle \Phi \rangle$ . We scale by units of standard deviations of the control-run to indicate how large the response is compared to the day-to-day variability at each level.

Fig. 5a shows the ensemble-mean of  $R$ , and Fig. 5b-d the evolution of  $R$  for selected individual realizations. In the ensemble- and time-mean, as expected from basic dynamical theory, the heights increase at almost all levels and times owing to the warming

from the dissipation of the planetary wave activity. Notice the delayed response of the upper stratosphere that is consistent with Fig. 4. After the initial forcing period at about day 20 the stratospheric anomalies decay slowly to zero with a timescale consistent with the 20-day thermal damping timescale. There is a subtle indication of downward propagation from the upper to the lower stratosphere, which is supported by the existence of small positive tropospheric height anomalies during day 60-80. However, a distinct stratosphere-to-troposphere downward propagating TST signal is missing.

*b. Classification of the realizations*

The lack of a signal that propagates back into the troposphere in the ensemble-mean reflects the fact that the tropospheric evolution of the perturbation integrations is highly variable from one realization to the next. The plots of  $R$  for the three individual realizations in Fig. 5b-d illustrate this spread. The timing, spatial pattern, and strength of those cases is very different, and bear little resemblance to the ensemble-mean (Fig. 5a). This high variability of individual outcomes is a signature of the strong nonlinearity of the extratropical circulation and its response to external perturbations, and is one of the main reasons why we have performed an ensemble calculation with so many realizations. Only by averaging over many members does the signal to noise ratio become sufficiently large. Looking over all the ensemble members, we find that a clear downward propagating signal, as for example exhibited by “case 43” (Fig. 5d), occurs in only about 1/3 of all cases. Even for those cases, the timing of the tropospheric return signal is again quite variable.

Despite the large spread, we find that we are able to classify the many different outcomes of our experiments into a few basic categories. Our classification scheme is

based on the time of the strongest tropospheric  $R$  signal for each realization. Excluding the time period of the initial tropospheric wave pulse, we divide the time interval of each realization into “early” (day 25-50), “intermediate” (day 51-75) and “late” (day 76-100) periods. We then calculate, for each realization, the value of the time-mean and tropospheric vertical-mean (specifically, the 191-853 hPa mean)  $R$  in each of these three periods. If the largest of these values occurs in the early, intermediate, or late period, we classify the realization as “E”, “I”, or “L”, respectively. Finally, we create composite averages over the E, I, and L groups of realizations.

We next exclude from our classification those members of the ensemble with a large initial AM value to bypass problems with the persistent behavior of the AM in this model. This behavior is demonstrated in Fig. 6a, which shows the evolution of tropospheric vertical-mean (97-853 hPa)  $R$  composites of those experiments that have initially a large negative ( $AM < -1$ ) or positive ( $AM > 1$ ) AM index. One can see that the tropospheric AM which is present in the initial conditions decays very slowly over time. This and other analysis we have pursued show that the AM and other aspects of the tropospheric high-latitude variability are unrealistically persistent in this model, with a decorrelation time-scale of about 100 days. This behavior is largely independent of the tropospheric wave activity pulse, as can be seen by comparing with Fig. 6b, which shows the tropospheric  $R$  taken from the corresponding cases in the control-run that are not forced by the tropospheric wave-activity pulse. The persistence implies that a realization that includes an initially strongly positive tropospheric AM state is picked up as an L event in our classification, and an initially strongly negative AM state as an E event, independently of the perturbation or of the stratospheric response. Neither case reflects stratosphere-to-

troposphere propagation, and so the persistent AM signals overwhelm the more subtle downward propagating signals. We choose a threshold initial AM index magnitude of  $2/3$  and exclude cases with an initial AM magnitude that exceeds this value. This removes about half of the available realizations and leaves 201 out of the original 403 cases.

The results of the classification are shown in Fig. 7. The panels on the left show the quantity  $R$  for each of the groups (with the averaging regions in time-pressure coordinates shown for reference), and the panels on the right show the difference between  $R$  for each of the group composites and the ensemble-mean value of  $R$ . The number above each panel indicates how many realizations fall in each group; the distribution of 79:63:59 is approximately equal among each of the E, I, and L categories. This classification scheme brings out better defined TST events, particularly for the I and L cases (Fig. 7c and e); these panels shows that the tropospheric anomalies in the day 80-100 are part of a large coherent pattern that starts in the upper stratosphere near the time of the initial pulse. The signal strength in the troposphere for all the composites is about 0.8 standard deviations. This translates into a geopotential height anomaly of about 40 m, and into a change in surface pressure of about 4 hPa.

The composite meridional structure of these events is shown in Fig. 8 as a sequence of 25-day time averages with the ensemble-mean removed. The E and L patterns are structurally similar but of opposite sign. Anomalies whose sign match the long-term tropospheric response first appear in the upper stratosphere (day 0-24), then spread slowly into the lower stratosphere (day 25-49 and 50-74), and finally fill almost the entire atmospheric column over the polar cap (day 75-99). In the final stage, the anomalies project strongly on the AM of the model, as a comparison with Fig. 2b shows.

*c. Predictors of the tropospheric response*

A key issue is whether predictors of the different tropospheric responses can be found in the atmospheric state at time zero, i.e., immediately prior to the time of the externally imposed perturbation. The thin contouring in the top two panels of Fig. 9 shows the E- and L-composites of the (unscaled) geopotential height differences from the ensemble-mean at the initial time. For the L composite, there is a negative center in the lower stratosphere/upper troposphere that is centered around 65N, and a dipole structure in the upper stratosphere with a positive center around 80N and a negative center around 40N. For the E composite, the centers are of opposite sign and at similar locations, but the upper stratospheric centers are weaker. The zonal-mean zonal wind composites (middle panels) show that the L composite has a relatively weak and poleward shifted stratospheric polar vortex (see also Fig. 2) and a complex tropospheric structure.

Not all the features in Fig. 9 are statistically significant. The thick black contours indicate regions where the magnitudes of the anomalies exceed 10% of the climatological standard deviation of the control-run. This is a rough measure of statistical significance of the pattern features in the figure, if one assumes that the anomaly of one individual experiment is significant if it exceeds one climatological standard deviation ( $\sigma$ ), and that the critical standard deviation of the ensemble-mean scales like  $\sigma_{EM} \sim \sigma/(n)^{1/2}$ , where  $n$  is the ensemble size. With roughly  $n=70$  realizations in each composite, this results in a critical value of about 10%. In the upper stratosphere, the relatively stronger initial anomalies in the L cases are more significant, by this measure, than in the E cases. This can also be seen in Fig. 7b and f at day 0 between 1 hPa and 10 hPa.

Since the zonal-mean eddy driving represents the tendency of the zonal-mean winds, its initial distribution might provide a predictor of the tropospheric response that is independent of the initial winds. The bottom panels of Fig. 9 show the composite EP-flux cross sections for the E and L cases, minus the ensemble-mean. The cross sections are generally noisy, especially in the troposphere, but show a large and coherent positive EP-flux divergence anomaly in the extratropical lower stratosphere for the L composite and a roughly equal and opposite anomaly for the E composite.

We now test to see whether the initial anomalies in Fig. 9 can be used to predict the tropospheric outcomes in Fig. 7. We focus on the L case because the L-composite anomalies in Fig. 9 are more statistically significant. Starting from the full 403 member ensemble, we first exclude the 202 realizations that project strongly onto the AM initially (for these realizations, the best tropospheric forecast is persistence of the initial AM anomalies). We plot the composite-mean  $R$ , with the ensemble-mean removed, for realizations whose initial conditions show anomalously positive high-latitude EP-flux divergence in the lower stratosphere (Fig. 10a), anomalously positive high-latitude geopotential in the upper stratosphere (Fig. 10b), or both (Fig. 10c). The panels in Fig. 10, which are based on a priori information (i.e., the initial conditions prior to the perturbation), can be compared to Fig. 7f, which is based on a posteriori information (i.e., the known outcomes). Although one criterion alone is unable to reproduce the characteristic downward propagating patterns, both criteria together are relatively successful in predicting the L-type tropospheric response.

*d. An independent test of the predictors*

The favorable comparison between Fig. 7f and Fig. 10c suggests that randomly chosen initial conditions that satisfy our two criteria on EP-flux divergence and upper-stratospheric wind lead fairly reliably to an L response. We now perform an additional test that better highlights the role of these criteria when they are very strongly satisfied. In this test, we perform a small number of additional perturbation experiments for the *deliberately* chosen initial states that most strongly satisfy the two criteria. We proceed as follows:

- First, we find periods in which the 10-day running average, 60N-90N mean EP-flux divergence at 80 hPa takes on a particularly large value of greater than  $10^{-5} \text{ m}\cdot\text{s}^{-2}$ . There are 29 such days in the control run. For this independent test, no pre-selection on AM strength is performed.
- Of these 29 days, we select six of these days in which the geopotential at high latitudes in the middle and upper troposphere exceeds +200m. This choice is somewhat subjective, since the requirement was fulfilled by more than six initial conditions. Fig. 11 presents the EP-flux, geopotential, and zonal-wind structure of these six states. Notice that the patterns are consistent with the L composite mean of Fig. 9b, d, and f, but that the anomaly amplitudes are approximately an order of magnitude larger for these six cases.
- Finally, we perform our standard perturbation experiments on these six initial states, but extend the integration time from 100 to 140 days, so that more details about the response at later times are captured. The panels on the left of Fig. 12 show the outcome of the perturbation experiments in terms of the quantity  $R$ , and



the bottom panel shows the ensemble-mean of  $R$  for the six runs. Each panel shows also a 20 day long history of  $R$  prior to the corresponding initial condition at day 0.

The selected initial conditions indeed tend to result in an L-type response, since five out of the six experiments show well defined stratosphere-to-troposphere signals which peaks in the troposphere at around day 100. The outcomes of the individual experiments bear also a striking resemblance with downward-propagating events in observations (e.g. Baldwin and Dunkerton 2001), in particular because of the familiar pattern that resembles “dripping paint”. The results can be compared with the panels on the right-hand side of Fig. 12, which shows the evolution of  $R$  for the corresponding cases of the unperturbed control-run. Interestingly, the control-run cases show also some tendency of weak downward propagation. This is probably related to the relatively warm upper stratospheric conditions prior to day 0, and weak pulses of upward propagating waves shortly before day 0. Such additional wave activity can be found in the  $R$ -signatures of all six cases, and leads to an upper-stratospheric warming that maximizes at day 0. The tendency for downward propagation seems to be amplified in the perturbation experiments by imposing additional wave forcing after day 0.

#### *e. Dynamical interpretation*

We may ask why the criteria we used in Fig. 10 would lead to a delayed tropospheric (L) response relative to the ensemble-mean:

1. *The L cases are favored by a weaker and poleward shifted upper stratospheric vortex (Fig. 9d).* This appears to cause more wave activity to be initially absorbed at higher levels in the stratosphere than in the ensemble-mean (see Fig. 7f). This, in turn, would delay the tropospheric response if the rate of downward descent of the

zonal-mean flow anomaly is roughly constant among the realizations: since the anomaly is starting at a higher level, it will take longer to descend to the surface.

2. *The L cases are also favored by anomalously positive EP-flux divergence in the lower stratosphere (Fig. 9f).* The EP-flux divergence signature seems to indicate that a wave activity anomaly has just propagated out of the lower stratosphere into the upper stratosphere, where it is causing eddy-induced warming. This is evident in Fig. 12, in which all the states have been "preconditioned" warm in the twenty days prior to time 0. The EP-flux divergence also implies that the lower stratospheric westerlies are set to strengthen after the main pulse is initiated. Linear theory suggests that less wave activity will be absorbed in the lower stratosphere than in the ensemble-mean as a result. Thus, more wave activity will be absorbed at higher levels, which is again consistent with the impact of the weaker and poleward-shifted vortex.

It is difficult to determine conclusively what the importance and dynamical interpretation of the initial *tropospheric* anomalies in Fig. 9 and Fig. 11 is. Thus, we cannot rule out the possibility that tropospheric initial conditions exert a significant, or even a major, influence on the upward propagating pulse, beyond the AM persistence.

#### **4. Conclusion**

We have used an externally imposed lower-tropospheric planetary-wave pulse in a simple GCM to generate troposphere-stratosphere-to-troposphere (TST) events in a controlled way. The ensemble-mean response, after the stratospheric warming, does not exhibit a distinct stratosphere-to-troposphere downward propagating signal. This is because the ensemble-mean averages over a broad range of responses whose

characteristics emerge when we separate cases with early (E) and late (L) times of a tropospheric return signal. We use the E/L classification to illustrate the typical life cycle of the stimulated TST events (Fig. 7 and Fig. 8). This framework allows us to determine which prior atmospheric conditions predict the tropospheric response (Section 3c).

We have found that realizations in which the tropospheric return signal is late (L) are favored by stratospheric conditions in which the wave activity pulse is absorbed at relatively high levels. Both the initial zonal-mean winds and the eddy forcing (related to the wind tendency) provide independent information about the likelihood of a late response. Our simple explanation for the timing of the tropospheric response, illustrated schematically in Fig. 13, is that the rate of downward descent does not vary systematically among the realizations, so that the signal arrives later in the troposphere if it is initially stimulated at higher levels in the stratosphere.

Just what controls the rate of downward descent of TST signals in this model and in the observations remains an open question. However, for realistic values of stratospheric thermal damping, we know that the rate of descent of TST signals should increase as the damping rate is increased. Two effects might be at work here, first, the fact that the phase speed of the linear adjustment of the zonal-mean circulation to stratospheric perturbations is proportional to the damping rate (Dickinson 1968, Haynes et al. 1991, KP), and second that the eddy driving of the mean flow is stronger if the damping rate is stronger (as in the weakly nonlinear theory of the quasi-biennial oscillation). Sorting out these issues is beyond the scope of this study, but to support the idea that the rate of downward descent is an increasing function of the damping rate, we show in Fig. 14 the results of additional perturbation-ensemble realizations in which the stratospheric damping rates are doubled

from 1/(20 d) to 1/(10 d) and halved from 1/(20 d) to 1/(40 d). The figure shows the frequency distribution of E, I, and L cases, and indeed supports the idea that stronger damping rates favor earlier tropospheric return signals, and weak damping rates favor later tropospheric return signals.

We have been particularly surprised at the variability of the response to the surface perturbation, as exemplified by Fig. 5, especially in light of our previous experience with generating upward propagating waves by perturbing the lower stratosphere (Polvani and Saravanan 2000, Scott et al. 2004). This variability is caused in the present study by the way the pulse interacts with the tropospheric circulation on the way to the stratosphere, and by the sensitivity of the stratospheric breaking to details of the polar-vortex structure. Given this uncertainty in the atmospheric response at early times (days 0-20), it is perhaps not surprising that the response at later times was found to be so highly variable.

## Appendix: Forcing of the model

We apply linear Rayleigh damping to the momentum equations using a damping coefficient  $k_v$  of

$$k_v(\sigma) = \begin{cases} k_f \frac{\sigma - \sigma_b}{1 - \sigma_b}, & \sigma > \sigma_b \\ k_{sp} \left( \frac{\sigma_{sp} - \sigma}{\sigma_{sp}} \right)^2, & \sigma < \sigma_{sp} \\ 0, & \text{else} \end{cases} \quad (\text{A1})$$

Following HS, we chose  $\sigma_b = 0.7$  ( $\sim 700$  hPa) and  $k_f = 1 \text{ day}^{-1}$  to mimic frictional effects in the planetary boundary layer. A sponge layer with  $\sigma_{sp} = 5 \cdot 10^{-4}$  ( $\sim 0.5$  hPa) and

$k_{sp} = 0.5 \text{ day}^{-1}$  is added at the model top to simulate gravity wave drag in the mesosphere and to prevent spurious wave reflection from the upper boundary.

We use Newtonian cooling to relax the temperatures  $T$  towards a prescribed equilibrium temperature profile  $T_{eq}$

$$\frac{\partial T}{\partial t} = \dots - k_T(\varphi, \sigma) [T - T_{eq}(\varphi, p)] \quad (\text{A2})$$

with a thermal relaxation coefficient  $k_T$  of

$$k_T(\varphi, \sigma) = \begin{cases} k_a + (k_s - k_a) \frac{\sigma - \sigma_b}{1 - \sigma_b} \cos^4 \varphi, & \sigma \geq \sigma_b \\ k_a, & \sigma_b > \sigma \geq \sigma_{s1} \\ k_{st} + (k_a - k_{st}) \frac{\sigma - \sigma_{s2}}{\sigma_{s1} - \sigma_{s2}}, & \sigma_{s1} > \sigma \geq \sigma_{s2} \\ k_{st}, & \sigma_{s2} > \sigma \end{cases} \quad (\text{A3})$$

In the troposphere ( $\sigma \geq \sigma_{s1}$ ) we use  $k_a = 1/(40 \text{ d})$  and  $k_s = 1/(4 \text{ d})$  as in the HS prescription. To match more closely observed stratospheric values (Dickinson 1968), we modify this prescription in the stratosphere so that  $k_T$  transitions as a linear function of sigma to a value of  $k_{st} = 1/(20 \text{ d})$  between  $\sigma_{s1}=0.15$  ( $\sim 150 \text{ hPa}$ ) and  $\sigma_{s2}=0.095$  ( $\sim 95 \text{ hPa}$ ), and  $k_T = k_{st} = 1/(20 \text{ d})$  above.

Following PK and KP, the equilibrium temperature profile  $T_{eq}$  is defined by

$$T_{eq}(\varphi, p) = \begin{cases} T_{eq}^{strat}(\varphi, p), & p < p_T \\ T_{eq}^{trop}(\varphi, p), & p \geq p_T \end{cases} \quad (\text{A4})$$

with latitude  $\varphi$ , pressure  $p$ , and a tropopause at  $p_T = 100 \text{ hPa}$ . The stratospheric relaxation temperature is given by

$$T_{eq}^{strat}(\varphi, p) = [1 - W(\varphi)] T_{US}(p) + W(\varphi) T_{PV}(p; \gamma), \quad (\text{A5})$$

where  $T_{US}(p)$  is taken from the temperature profile of the U.S. Standard Atmosphere (COESA 1976), and

$$T_{PV}(p; \gamma) = T_{US}(p_T) \left( p / p_T \right)^{\frac{R\gamma}{g}}, \quad (\text{A6})$$

is the temperature of an atmosphere with constant lapse rate  $\gamma$ , and standard notation otherwise. The parameter  $\gamma$  which controls the strength of the stratospheric temperature gradient over the winter pole (PK), is set to 1 K/km. The weight function

$$W(\varphi) = \frac{1}{2} \left[ 1 + \tanh \left( \frac{\varphi - \varphi_0}{\Delta\varphi} \right) \right], \quad (\text{A7})$$

is used to confine the cooling over the winter pole. With  $\varphi_0 = 50^\circ\text{N}$  and  $\Delta\varphi = 10^\circ\text{N}$  latitude,  $T_{eq}^{strat}$  varies smoothly from a cold stratosphere over the high latitudes of the winter (northern) hemisphere to the US Standard Atmosphere over all other latitudes. The tropospheric relaxation temperature  $T_{eq}^{trop}$  is defined by

$$T_{eq}^{trop}(\varphi, p) = \max \left[ T_{US}(p_T), (T_0 - \delta T) \left( p / p_0 \right)^\kappa \right], \quad (\text{A8})$$

where  $T_0 = 315^\circ\text{K}$ ,  $p_0 = 1000$  hPa, and  $\kappa = 2/7$ , with

$$\delta T = \delta_y \sin^2 \varphi + \varepsilon \sin \varphi + \delta_z \cos^2 \varphi \log(p / p_0) \quad (\text{A9})$$

where  $\delta_y = 60^\circ\text{K}$ ,  $\delta_z = 10^\circ\text{K}$ , and  $\varepsilon = 0$ . With this choice of parameters the tropospheric equilibrium temperature profile is identical to the HS benchmark.

## References

Ambaum, M. H. P. and B. J. Hoskins, 2002: The NAO Troposphere–Stratosphere Connection. *J. Climate*, **15**, 1969–1978.

- Andrews, D. G., J. R. Holton, and C. B. Leovy, 1987: *Middle Atmosphere Dynamics*. Academic Press.
- Baldwin, M. P. and T. J. Dunkerton, 1989: The stratospheric major warming of early December 1987. *J. Atmos. Sci.*, **46**, 2863–2884.
- Baldwin, M. P. and T. J. Dunkerton, 1999: Propagation of the Arctic Oscillation from the stratosphere to the troposphere. *J. Geophys. Res.-Atmos.*, **104**, 30937-30946.
- Baldwin, M. P. and T. J. Dunkerton, 2001: Stratospheric harbingers of anomalous weather regimes. *Science*, **294**, 581-584.
- Baldwin, M. P., D. W. J. Thompson, E. F. Shuckburgh, W. A. Norton, and N. P. Gillett, 2003: Weather from the Stratosphere? *Science*, **301**, 317-319.
- Black, R. X., 2002: Stratospheric Forcing of Surface Climate in the Arctic Oscillation. *J. Climate*, **15**, 268–277.
- Charlton, A. J., A. O. O'Neill, W. A. Lahoz, and A. C. Massacand, 2004: Sensitivity of tropospheric forecasts to stratospheric initial conditions. *Quart. J. Roy. Meteor. Soc.*, (submitted).
- Charney, J. G. and P. G. Drazin, 1961: Propagation of planetary-scale disturbances from the lower into the upper atmosphere. *J. Geophys. Res.*, **66**, 83-109.
- Christiansen, B., 2003: Temporal growth and vertical propagation of perturbations in the winter atmosphere. *Quart. J. Roy. Meteor. Soc.*, **129**, 1589.
- COESA, 1976: *U.S. Standard Atmosphere*. U.S. Government Printing Office, 227 pp.
- Dickinson, R. E., 1968: On the excitation and propagation of zonal winds in an atmosphere with Newtonian cooling. *J. Atmos. Sci.*, **25**, 269–279.

- Gillett, N. P. and D. W. J. Thompson, 2003: Simulation of recent southern hemisphere climate change. *Science*, **302**, 273-275.
- Haynes, P. H., M. E. McIntyre, T. G. Shepherd, C. J. Marks, and K. P. Shine, 1991: On the “downward control” of extratropical diabatic circulations by eddy-induced mean zonal forces. *J. Atmos. Sci.*, **48**, 651–680.
- Held, I. M. and M. J. Suarez, 1994: A proposal for the intercomparison of the dynamical cores of atmospheric general circulation models. *Bull. Amer. Meteor. Soc.*, **75**, 1825–1830.
- Holton, J. R. and C. Mass, 1976: Stratospheric vacillation cycles. *J. Atmos. Sci.*, **33**, 2218–2225.
- Kushner, P. J. and L. M. Polvani, 2004: Stratosphere–troposphere coupling in a relatively simple AGCM: The role of eddies. *J. Climate*, **17**, 629–639.
- Matsuno, T., 1971: A dynamical model of the stratospheric sudden warming. *J. Atmos. Sci.*, **28**, 1479–1494.
- McIntyre, M. E. and T. N. Palmer, 1984: The "surf zone" in the stratosphere. *J. Atmos. Terr. Phys.*, **46**, 825-849.
- Perlwitz, J. and N. Harnik, 2003: Observational evidence of a stratospheric influence on the troposphere by planetary wave reflection. *J. Climate*, **16**, 3011–3026.
- Plumb, R. A. and K. Semeniuk, 2003: Downward migration of extratropical zonal wind anomalies. *J. Geophys. Res.*, **108** (D7), 4223, doi:10.1029/2002JD002773.
- Polvani, L. M. and R. Saravanan, 2000: The three-dimensional structure of breaking Rossby waves in the polar wintertime stratosphere. *J. Atmos. Sci.*, **57**, 3663–3685.



- Polvani, L. M. and P. J. Kushner, 2002: Tropospheric response to stratospheric perturbations in a relatively simple general circulation model. *Geophys. Res. Lett.*, **29**, 10.1029/2001GL014284.
- Polvani, L. M. and D. W. Waugh, 2004: Upward wave activity flux as precursor to extreme stratospheric events and subsequent anomalous surface weather regimes. *J. Climate*, (accepted).
- Scinocca, J. F. and P. H. Haynes, 1998: Dynamical forcing of stratospheric planetary waves by tropospheric baroclinic eddies. *J. Atmos. Sci.*, **55**, 2361–2392.
- Scott, R. K., D. G. Dritschel, L. M. Polvani, and D. W. Waugh, 2004: Enhancement of Rossby Wave Breaking by Steep Potential Vorticity Gradients in the Winter Stratosphere. *J. Atmos. Sci.*, **61**, 904–918.
- Song, Y. and W. A. Robinson, 2004: Dynamical mechanism for stratospheric influences on the troposphere. *J. Atmos. Sci.*, (in press).
- Thompson, D. W. J. and S. Solomon, 2002: Interpretation of recent Southern Hemisphere climate change. *Science*, **296**, 895-899.

## Figure Captions

Fig. 1. Schematic illustration of the TST events simulated in this study: (1) Forced pulse of planetary waves occurring over time  $\Delta t$ ; (2) upward propagating waves; (3) dissipation and breaking of waves; (4) induced downward propagating anomalies; (5) tropospheric response at time lag  $\tau > \Delta t$ .

Fig. 2. Time- and zonal-mean fields as a function of latitude and pressure derived from the control experiment. (a) Zonal wind in  $\text{m s}^{-1}$ . (b) Pattern of the annular mode in  $\text{m}$ . Here and elsewhere negative contours are dashed.

Fig. 3. The ensemble-mean departure of the 116 hPa geopotential height field from the control-run during the peak response at this level (day 8).

Fig. 4. The potential vorticity field on the 950-K potential temperature surface (ca. 5 hPa) in a stereographic projection. Shown is (a) the time-mean of the control-run, and (b) the ensemble-mean of the perturbation experiments during the peak response at this level (day 15). Units are potential vorticity units ( $1 \text{ PVU} = 10^{-6} \text{ m}^2 \text{ s}^{-1} \text{ K kg}^{-1}$ ).

Fig. 5. The quantity  $R$  in eqn. (4) as a function of time and pressure.  $R$  represents normalized geopotential height anomalies averaged over the polar cap (see text for details) Shown are (a) the ensemble-mean over all 403 realizations, and (b)-(d) individual selected cases.

Fig. 6. The composite temporal evolution of  $R$  (vertically averaged from 191 to 853 hPa) for realizations with a strongly negative (continuous line) or strongly positive (dashed line) annular mode index (vertically averaged from 97 to 853 hPa) at  $t=0$ .

(a) For members of the perturbation ensemble, and (b) for the corresponding members of the unperturbed control-run.

Fig. 7. The classification of the perturbation experiments into (top) E, (middle) I, and (bottom) L cases. The classification is based on the strongest  $R$  response averaged over the indicated regions (bold). Shown are (left) composites of  $R$  as a function of time and pressure and (right)  $R$  minus  $R_{EM}$ , the mean over the members of all three cases. The numbers above each panel indicate how many realizations fall into each case.

Fig. 8. The composite meridional structure of geopotential for the (top) E and (bottom) L cases in sequences of 25-day time averages. Shown are composite geopotential heights minus the mean over the members of all three cases as a function of latitude and pressure for day 0-24, 25-49, 50-74, and 75-99.

Fig. 9. The composite meridional structure of anomalies at the initial time for members of the (left) E and (right) L group. The anomalies are taken with respect to the mean over the realization of all three cases at the initial time. The thick black contours represents regions where the magnitude of the anomalies exceed 10% of the climatological standard deviation of the control-run, indicating that the anomalies are statistically significant. Shown are (top) geopotential heights in m, (middle) zonal winds in m/s, and (bottom) EP-flux divergence (contours) and EP-flux vectors (arrows). The divergence is divided by  $(a \cos(\phi))$  to show the acceleration of the zonal-mean flow (in  $10^{-7} \text{ m s}^{-2}$ ). The vectors are appropriately scaled to provide an idea of the relative size and sign of the vector components.

Fig. 10. Composites of  $R$  as a function of time and pressure minus the ensemble-mean response for realizations with the following high-latitude (60N-90N mean) initial conditions: (a) anomalously positive EP-flux divergence at 80 hPa, (b) anomalously positive zonal-mean geopotential at 3 hPa, and (c) both conditions.

Fig. 11. The meridional structure of six initial conditions from the control-run that fulfill the criteria of an L-type response. Shown are the anomalies of (left) anomalous EP-flux divergence, (middle) geopotential height, and (right) zonal wind. The anomalies are taken with respect to the climatological mean of the control-run. The bottom row shows the ensemble-mean of all six initial conditions. The contour levels are (left)  $\pm 5, \pm 10, \pm 20, \pm 40, \pm 80, \pm 160 \times 10^{-6} \text{ m/s}^2$ , (middle)  $\pm 50, \pm 100, \pm 200, \pm 400, \pm 800 \text{ m}$ , and (right)  $\pm 2, \pm 5, \pm 10, \pm 20, \pm 30 \text{ m/s}$ .

Fig. 12. The quantity  $R$  as a function of time (from day  $-20$  to  $+140$ ) and pressure for simulations using the six selected initial conditions ( $t=0$ ) shown in Fig. 1. The left panels are for perturbation experiments starting from those initial conditions (forced from day 0 to 10), and the right panels are for the unperturbed control-run in the absence of the wave-activity pulse. The bottom panels show the mean response of all six outcomes. The contour levels are identical to Fig. 5.

Fig. 13. Schematic illustration of how the timing of the tropospheric response is determined by the level of maximum eddy driving in the stratosphere.

Fig. 14. The frequency distribution of E, I, and L cases for different values of the stratospheric damping rate  $k_s$ . The distributions for  $k_s=1/(10 \text{ d})$  and  $1/(40 \text{ d})$  are derived from additional perturbation experiments with ensemble sizes of 101, and

the distribution for  $k_s=1/(20 \text{ d})$  comes from the standard perturbation experiment of this study with 403 members (Fig. 7). As for Fig. 7, realizations with a large initial AM are excluded for the calculation of the distributions.

## Figures

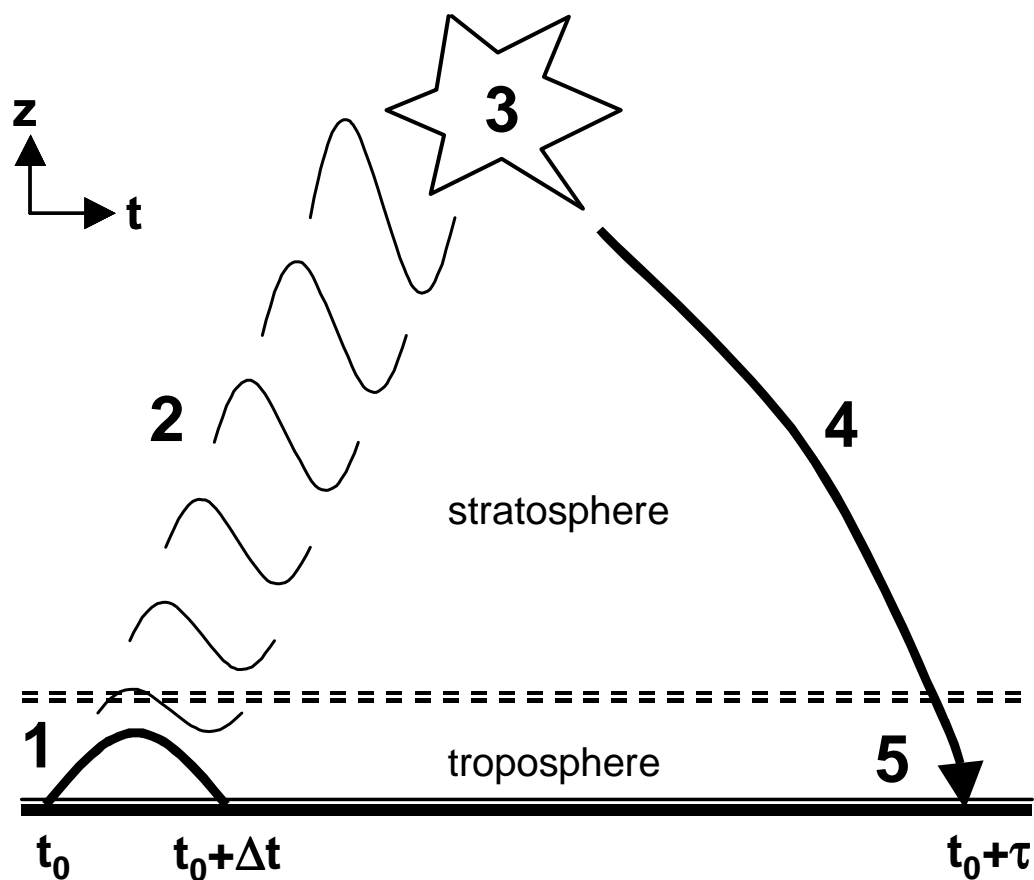


Fig. 1. Schematic illustration of the TST events simulated in this study: (1) Forced pulse of planetary waves occurring over time  $\Delta t$ ; (2) upward propagating waves; (3) dissipation and breaking of waves; (4) induced downward propagating anomalies; (5) tropospheric response at time lag  $\tau > \Delta t$ .

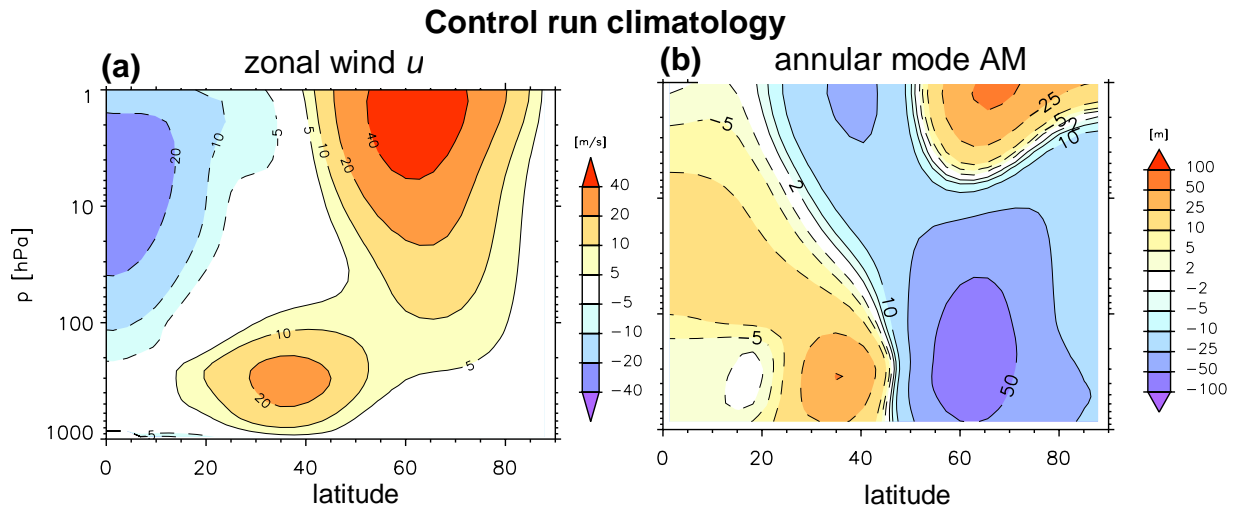


Fig. 2. Time- and zonal-mean fields as a function of latitude and pressure derived from the control experiment. (a) Zonal wind in  $m\ s^{-1}$ . (b) Pattern of the annular mode in  $m$ . Here and elsewhere negative contours are dashed.

**Z'** response: p = 116 hPa, t = day 8

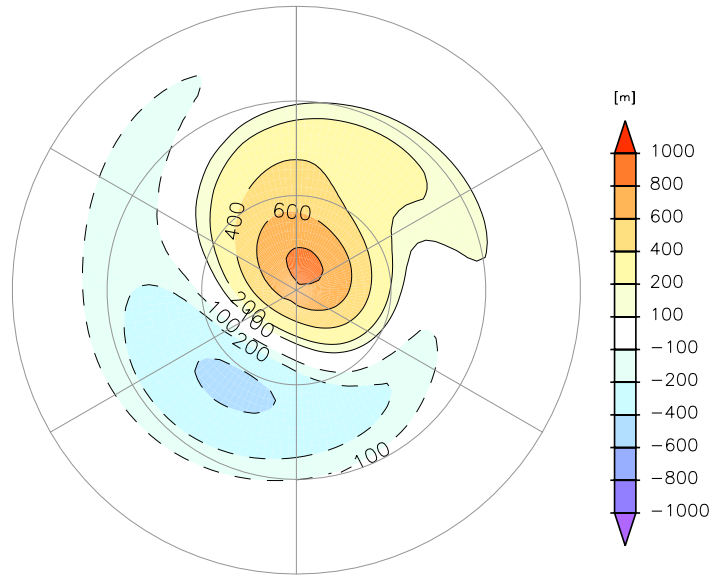


Fig. 3. The ensemble-mean departure of the 116 hPa geopotential height field from the control-run during the peak response at this level (day 8).



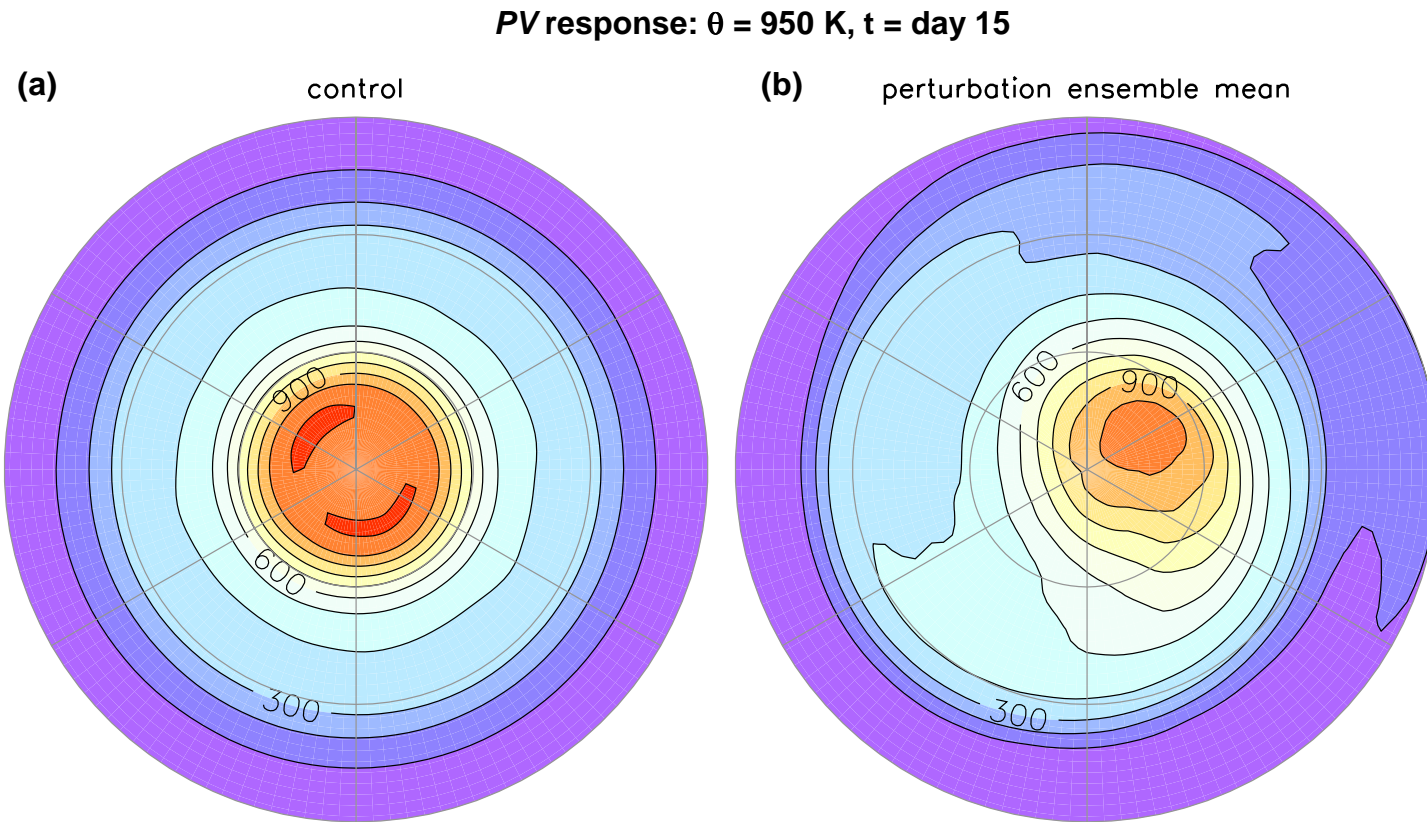


Fig. 4. The potential vorticity field on the 950-K potential temperature surface (ca. 5 hPa) in a stereographic projection. Shown is (a) the time-mean of the control-run, and (b) the ensemble-mean of the perturbation experiments during the peak response at this level (day 15). Units are potential vorticity units ( $1 \text{ PVU} = 10^{-6} \text{ m}^2 \text{ s}^{-1} \text{ K kg}^{-1}$ ).

## Geopotential response $R$

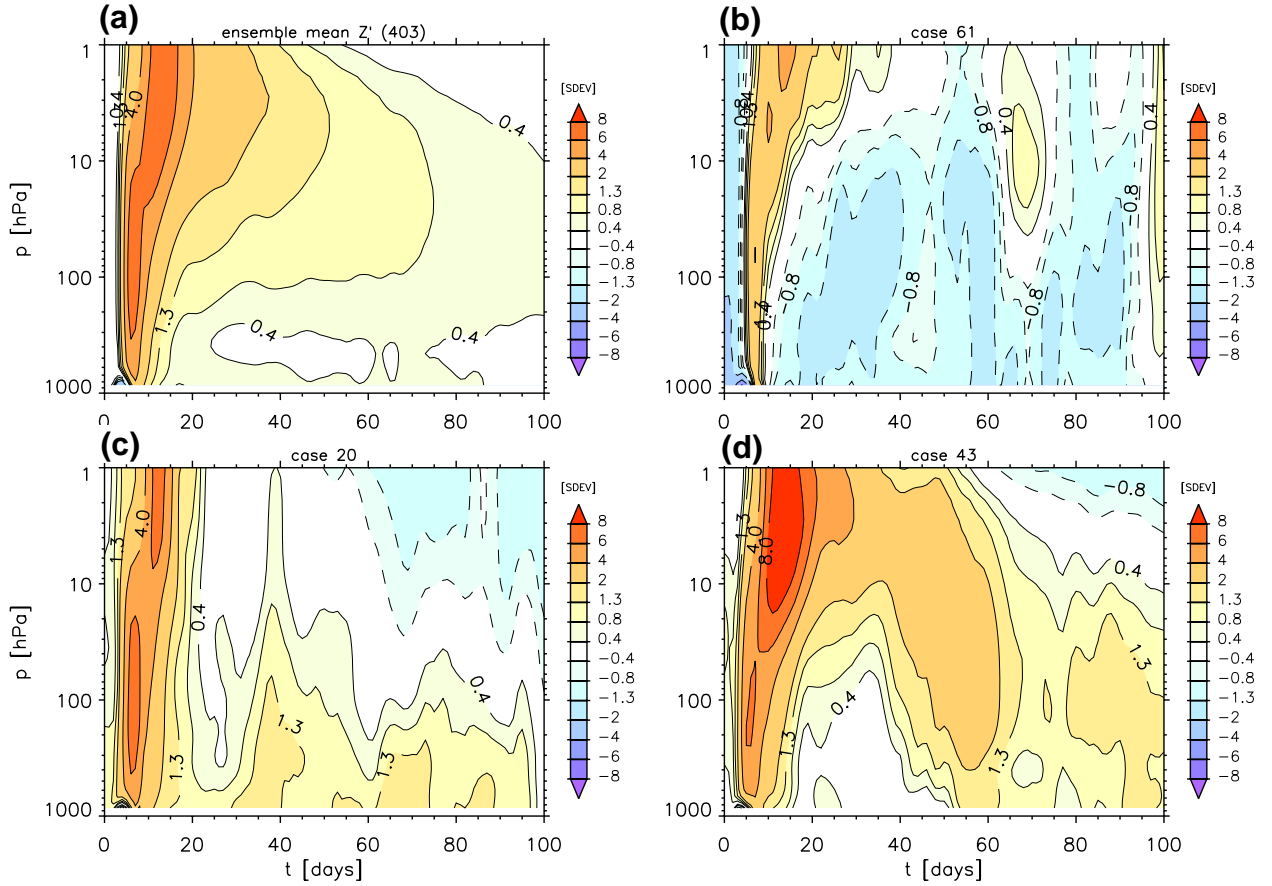


Fig. 5. The quantity  $R$  in eqn. (4) as a function of time and pressure.  $R$  represents normalized geopotential height anomalies averaged over the polar cap (see text for details) Shown are (a) the ensemble-mean over all 403 realizations, and (b)-(d) individual selected cases.

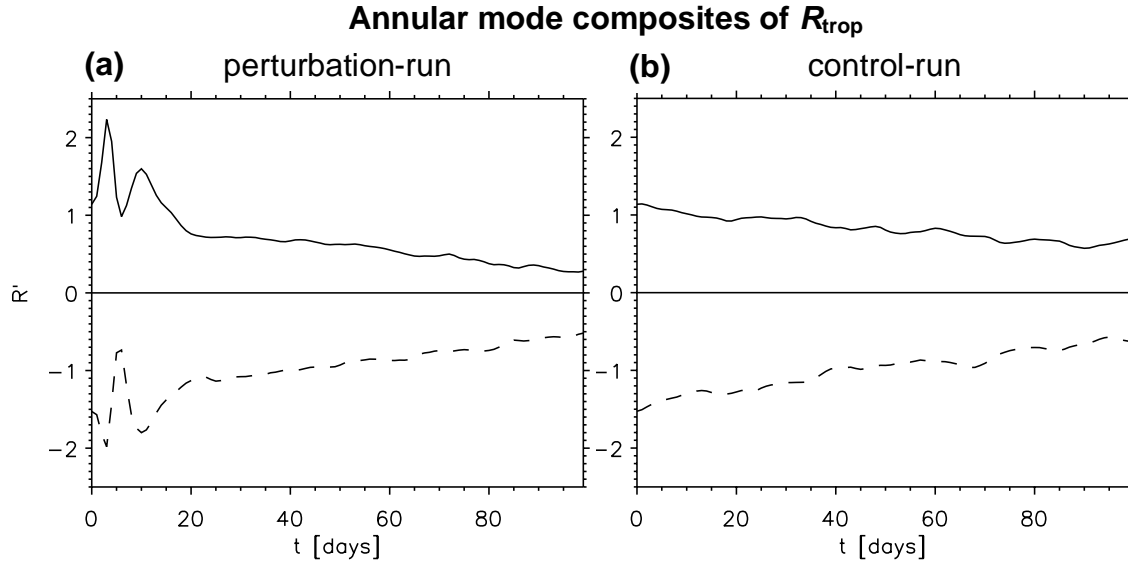


Fig. 6. The composite temporal evolution of  $R$  (vertically averaged from 191 to 853 hPa) for realizations with a strongly negative (continuous line) or strongly positive (dashed line) annular mode index (vertically averaged from 97 to 853 hPa) at  $t=0$ . (a) For members of the perturbation ensemble, and (b) for the corresponding members of the unperturbed control-run.

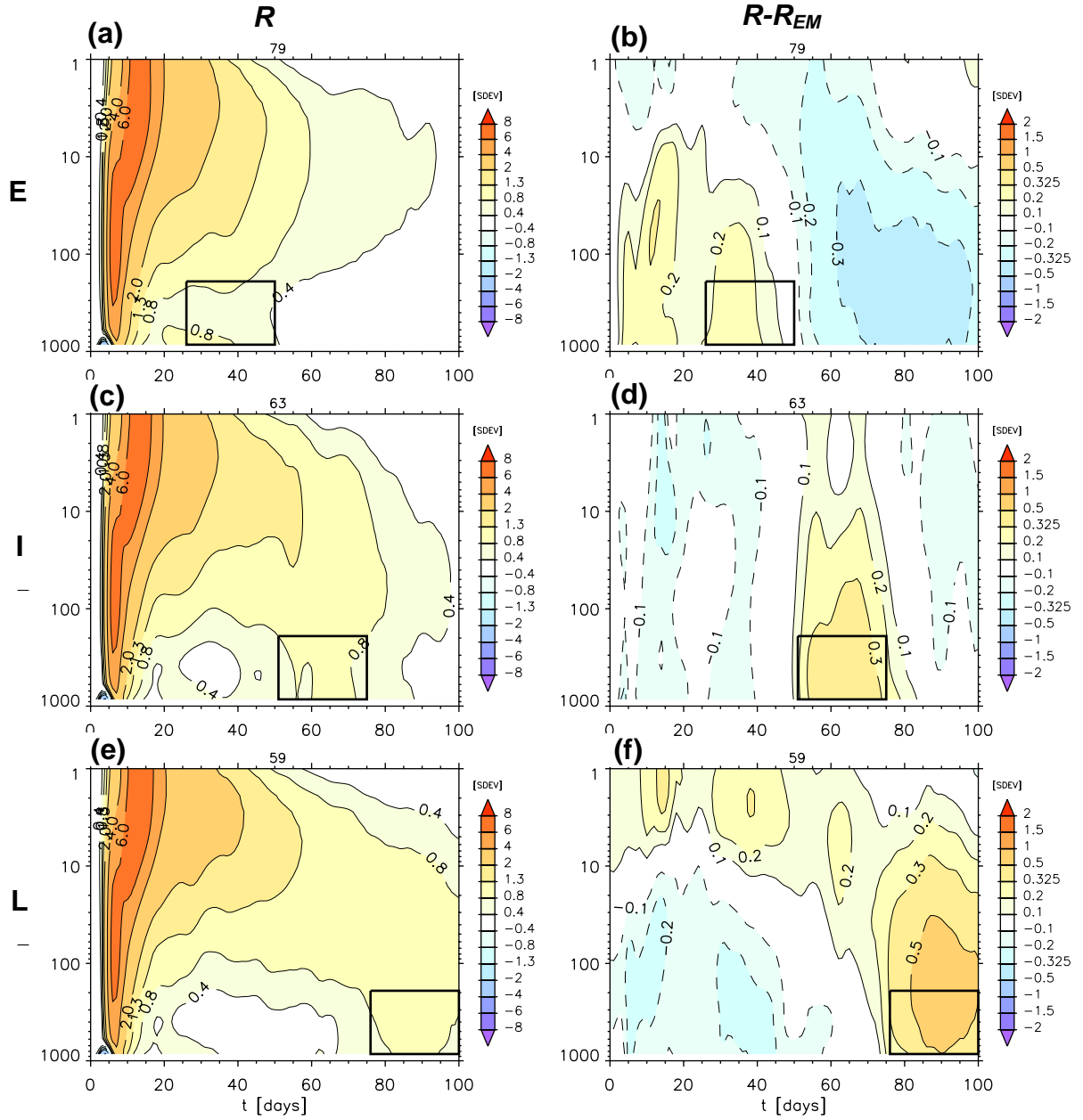


Fig. 7. The classification of the perturbation experiments into (top) E, (middle) I, and (bottom) L cases. The classification is based on the strongest  $R$  response averaged over the indicated regions (bold). Shown are (left) composites of  $R$  as a function of time and pressure and (right)  $R$  minus  $R_{EM}$ , the mean over the members of all three cases. The numbers above each panel indicate how many realizations fall into each case.

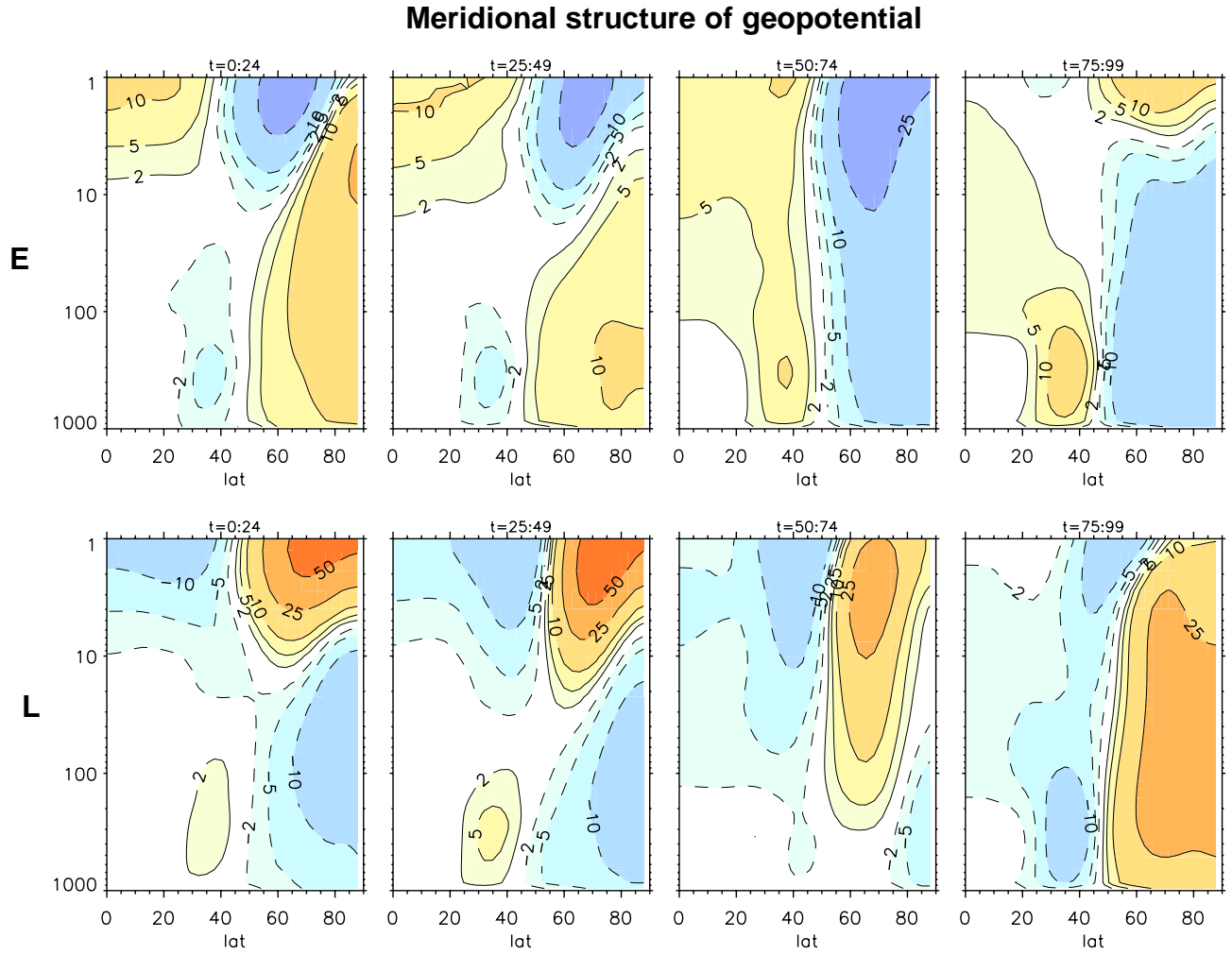


Fig. 8. The composite meridional structure of geopotential for the (top) E and (bottom) L cases in sequences of 25-day time averages. Shown are composite geopotential heights minus the mean over the members of all three cases as a function of latitude and pressure for day 0-24, 25-49, 50-74, and 75-99.



Fig. 9. The composite meridional structure of anomalies at the initial time for members of the (left) E and (right) L group. The anomalies are taken with respect to the mean over the realization of all three cases at the initial time. The thick black contours represents regions where the magnitude of the anomalies exceed 10% of the climatological standard deviation of the control-run, indicating that the anomalies are statistically significant. Shown are (top) geopotential heights in m, (middle) zonal winds in m/s, and (bottom) EP-flux divergence (contours) and EP-flux vectors (arrows). The divergence is divided by  $(a \cos(\phi))$  to show the acceleration of the zonal-mean flow (in  $10^{-7} \text{ m s}^{-2}$ ). The vectors are appropriately scaled to provide an idea of the relative size and sign of the vector components.

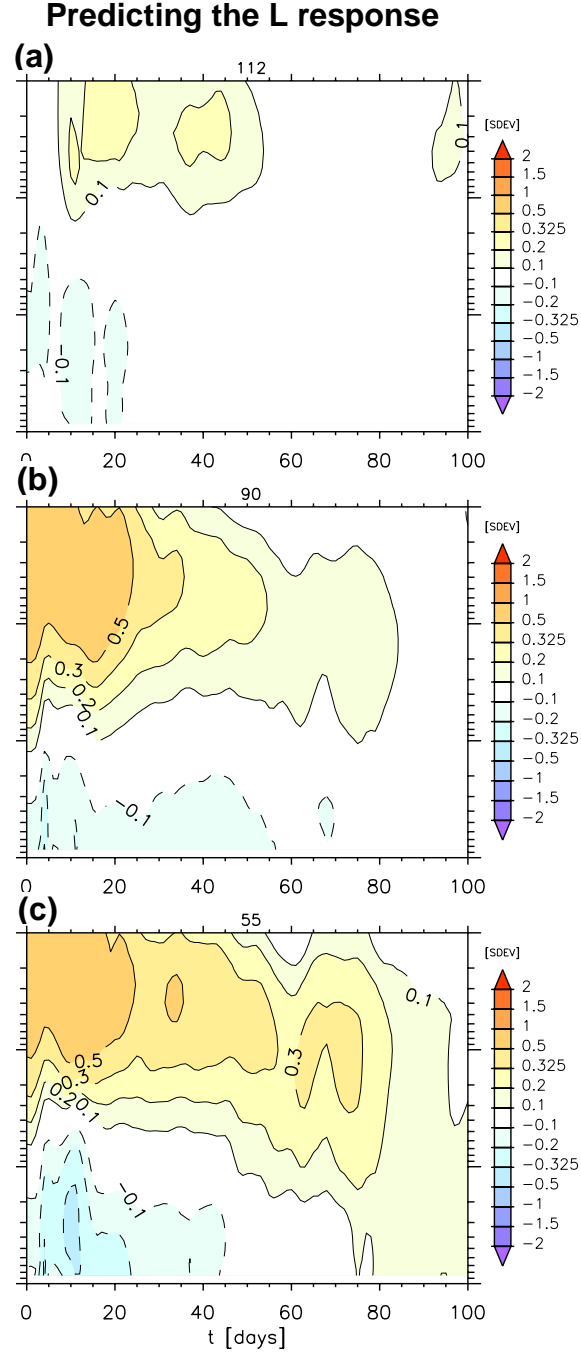


Fig. 10. Composites of  $R$  as a function of time and pressure minus the ensemble-mean response for realizations with the following high-latitude (60N-90N mean) initial conditions: (a) anomalously positive EP-flux divergence at 80 hPa, (b) anomalously positive zonal-mean geopotential at 3 hPa, and (c) both conditions.



## Selected initial conditions

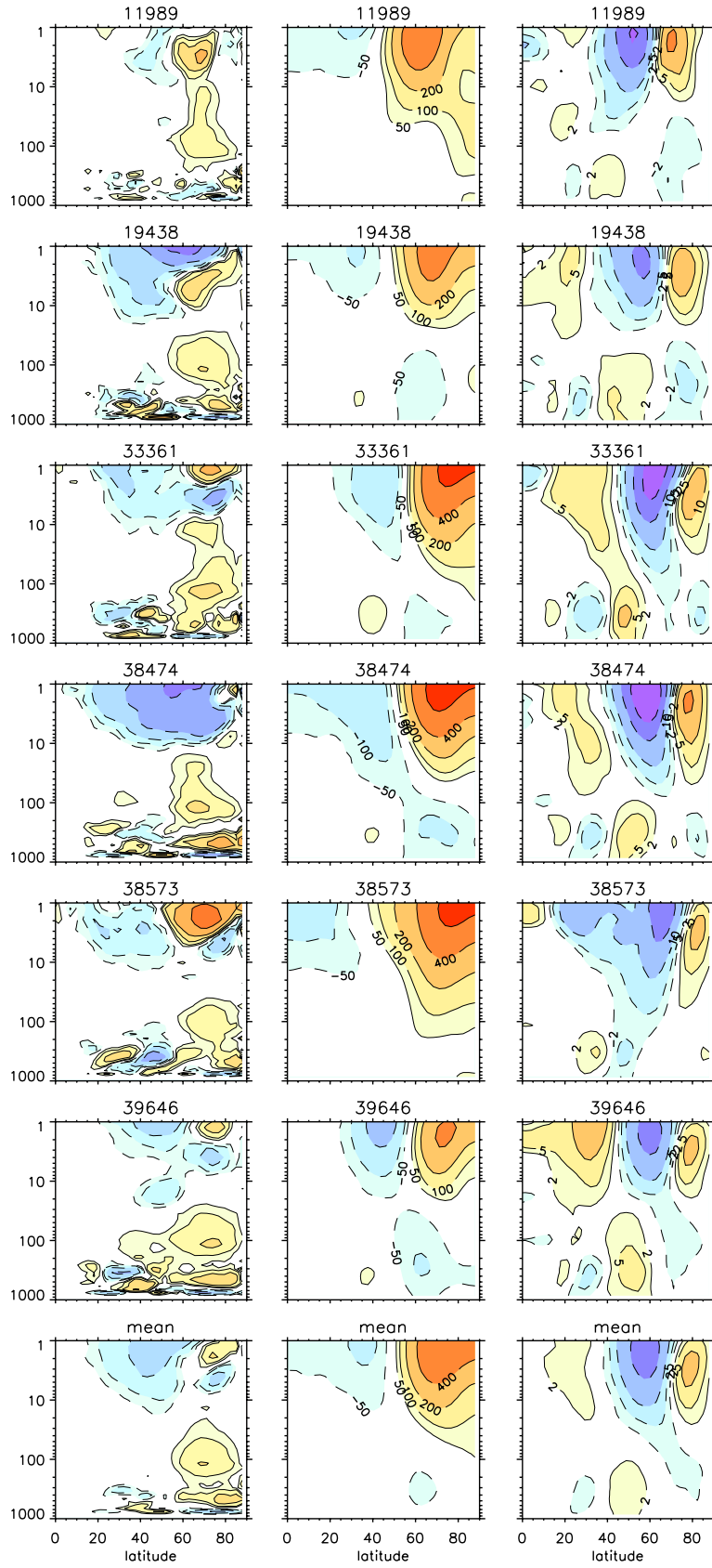


Fig. 11. The meridional structure of six initial conditions from the control-run that fulfill the criteria of an L-type response. Shown are the anomalies of (left) anomalous EP-flux divergence, (middle) geopotential height, and (right) zonal wind. The anomalies are taken with respect to the climatological mean of the control-run. The bottom row shows the ensemble-mean of all six initial conditions. The contour levels are (left)  $\pm 5, \pm 10, \pm 20, \pm 40, \pm 80, \pm 160 \times 10^{-6} \text{ m/s}^2$ , (middle)  $\pm 50, \pm 100, \pm 200, \pm 400, \pm 800 \text{ m}$ , and (right)  $\pm 2, \pm 5, \pm 10, \pm 20, \pm 30 \text{ m/s}$ .

## Response $R$

Perturbation experiments

Control run

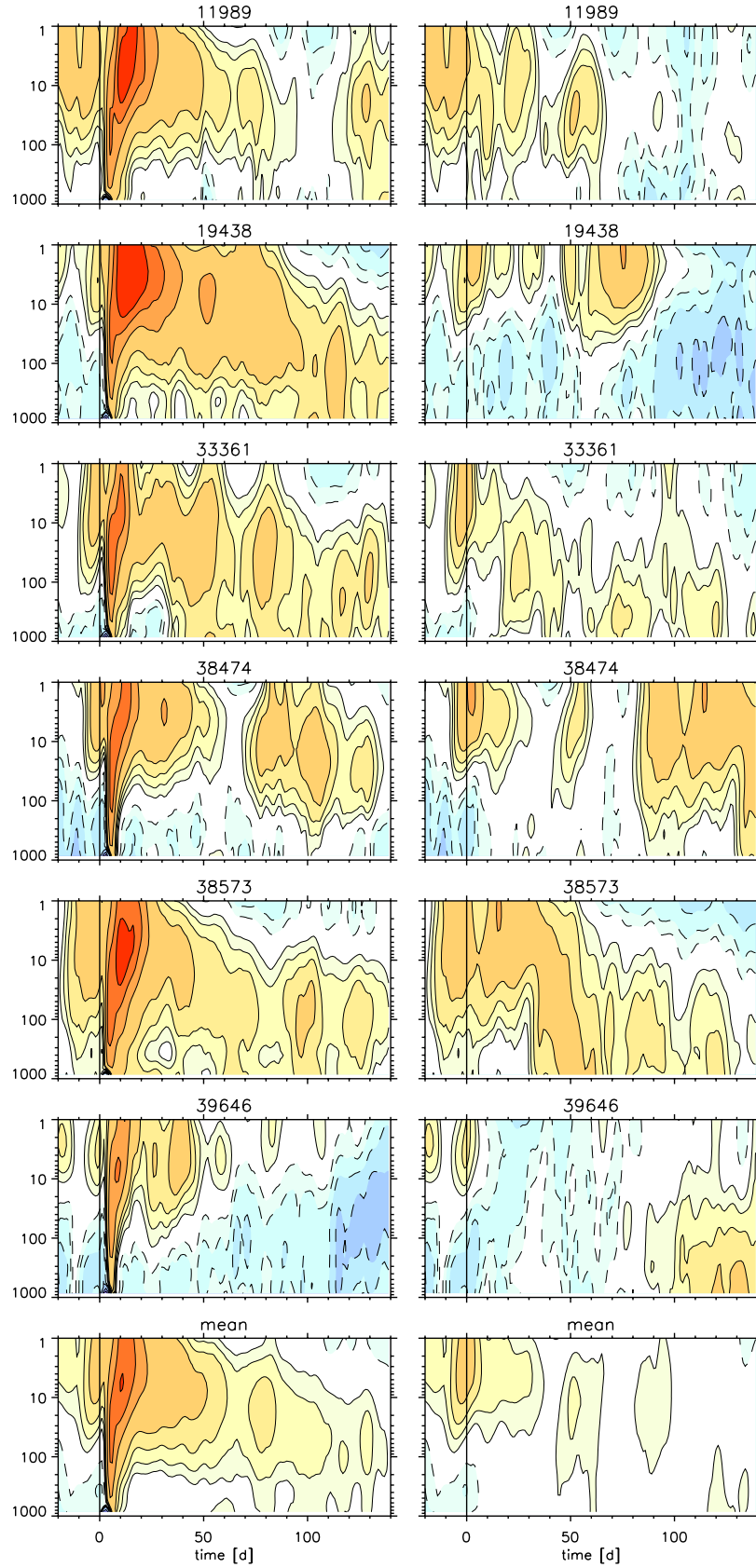


Fig. 12. The quantity  $R$  as a function of time (from day  $-20$  to  $+140$ ) and pressure for simulations using the six selected initial conditions ( $t=0$ ) shown in Fig. 1. The left panels are for perturbation experiments starting from those initial conditions (forced from day 0 to 10), and the right panels are for the unperturbed control-run in the absence of the wave-activity pulse. The bottom panels show the mean response of all six outcomes. The contour levels are identical to Fig. 5.

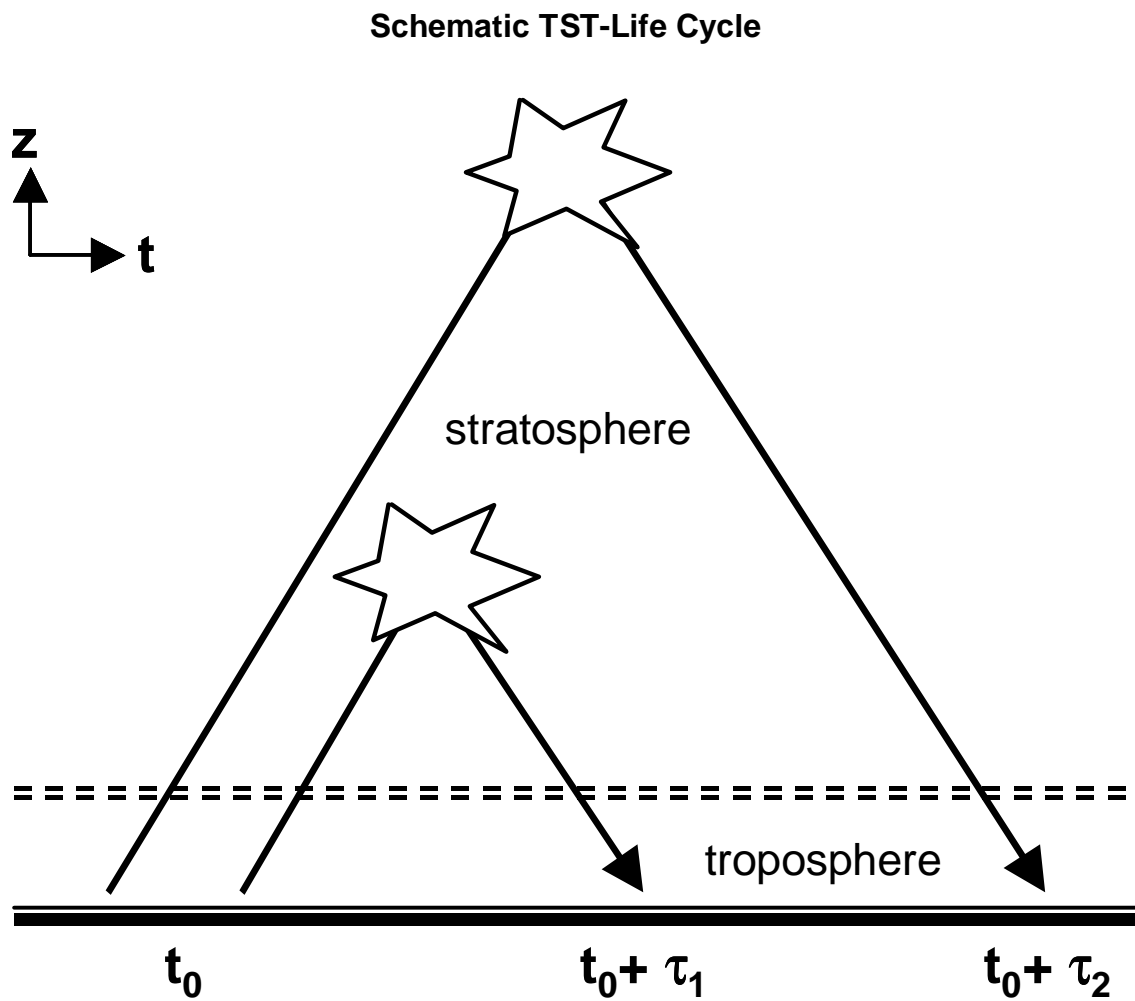


Fig. 13. Schematic illustration of how the timing of the tropospheric response is determined by the level of maximum eddy driving in the stratosphere.

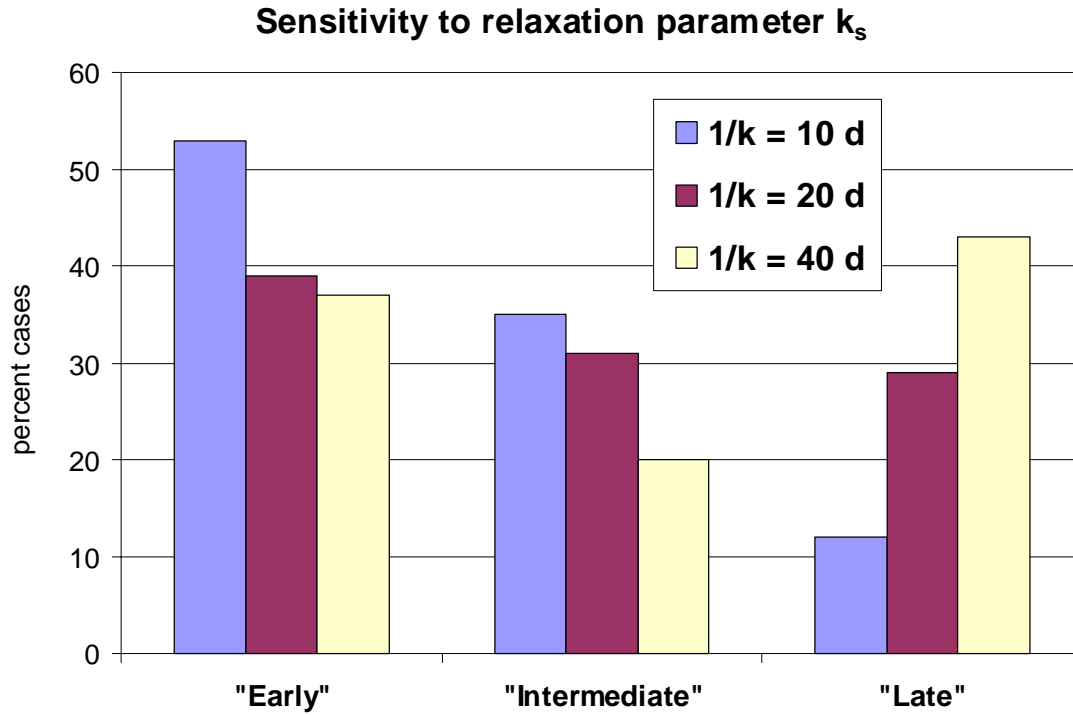


Fig. 14. The frequency distribution of E, I, and L cases for different values of the stratospheric damping rate  $k_s$ . The distributions for  $k_s=1/(10 \text{ d})$  and  $1/(40 \text{ d})$  are derived from additional perturbation experiments with ensemble sizes of 101, and the distribution for  $k_s=1/(20 \text{ d})$  comes from the standard perturbation experiment of this study with 403 members (Fig. 7). As for Fig. 7, realizations with a large initial AM are excluded for the calculation of the distributions.